ADVANCED FUNCTIONAL MATERIALS

Supporting Information

for *Adv. Funct. Mater.*, DOI 10.1002/adfm.202305283

Contrasting Charge-Carrier Dynamics across Key Metal-Halide Perovskite Compositions through In Situ Simultaneous Probes

Aleksander M. Ulatowski, Karim A. Elmestekawy, Jay B. Patel, Nakita K. Noel, Siyu Yan, Hans Kraus, Peter G. Huggard, Michael B. Johnston and Laura M. Herz**

Supporting Information: Contrasting charge-carrier dynamics across key metal halide perovskite compositions through in-situ simultaneous probes

Aleksander M. Ulatowski Karim A. Elmestekawy Jay B. Patel Nakita K. Noel Siyu Yan Hans Kraus Peter G. Huggard Michael B. Johnston Laura M. Herz**

A. M. Ulatowski, K. A. Elmestekawy, Dr. J. B. Patel, Dr. N. K. Noel, S. Yan, Prof. H. Kraus, Prof. M. B. Johnston, Prof. L. M. Herz
Department of Physics, University of Oxford, Clarendon Laboratory, Parks Road, Oxford, OX1 3PU, UK Email Address: laura.herz@physics.ox.ac.uk, michael.johnston@physics.ox.ac.uk
Prof. L. M. Herz
Institute for Advanced Study, Technical University of Munich, Lichtenbergstrasse 2a, D-85748 Garching, Germany
Prof. P.G. Huggard
STFC RAL Space, Rutherford Appleton Laboratory, Harwell, Didcot, OX11 0QX, UK

Contents

S1 Charge-carrier recombination modelling

The time evolution of photoconductivity transients (shown in Figures S1 and S3 of the SI, as well as in Figure 1 of the main text) was fitted with Equation 2 in the main text ($\sigma = \frac{\mu_{cc}}{2}(n+p)$) globally across all excitation fluences at each temperature. A numerical solution to the coupled rate equations (Equation 1a and 1b in the main text) was used to obtain the evolution of the charge-carrier density (n and p for the electron and hole populations, respectively) with time. The parameters extracted from the fits are listed in Tables S1 and S2 for $FA_{0.83}Cs_{0.17}PbBr_{0.6}I_{2.4}$ and $MAPbI_3$ thin films, respectively. The bimolecular recombination constants k_{Bi} shown in the tables were also plotted against temperature in Figures 2 and 3 of the main text. The boundary conditions used to solve numerically the coupled differential Equations 1a and 1b were as follows. (i) n_T, the number of trapped electrons, was set to 0 at time=0 of the decay since no electrons are present in the trap states prior to photoexcitation. The low repetition rate of the laser used to photoexcite the samples (5 kHz) ensured that sufficient time was given for any trapped charge carriers to relax to their respective bands between the excitation pulses. (ii) n, the number density of free electrons in the conduction band at time=0 of the decay was set to the photoexcited charge-carrier pair density, estimated from the excitation fluence, assuming that each absorbed photon generated one electron-hole pair. This assumption is highly accurate at high temperatures in metal halide perovskites owing to their low exciton binding energy and therefore high photon–to–free-carrier branching ratio ϕ, but as shown in Section S6.2 of the SI, the assumption might be inaccurate at low temperatures, <100 K, where significant exciton formation can occur [1]. The calculated photoexcited charge-carrier density is described by [2]

$$n(0) = \frac{F\lambda(1-R-T)\phi}{hcd}, \tag{S1}$$

where F and λ are the fluence and wavelength of the excitation pulse, respectively (400 nm central wavelength for excitation of $CsPbBr_3$, and 670 nm for $MAPbI_3$ and $FA_{0.83}Cs_{0.17}PbBr_{0.6}I_{2.4}$), and R and T are the fractions of reflected and transmitted photons at the excitation wavelength, respectively. The values of $(1-R-T)$ were calculated from the absorption measurement data to be 0.59, 0.69, and 0.77 for $FA_{0.83}Cs_{0.17}PbBr_{0.6}I_{2.4}$, $MAPbI_3$, and $CsPbBr_3$, respectively. The film thickness d was measured to be 320 nm, 320 nm, and 650 nm for $FA_{0.83}Cs_{0.17}PbBr_{0.6}I_{2.4}$, $MAPbI_3$, and $CsPbBr_3$, respectively. h represents the Plank constant and c is the speed of light. We note that the total time-dependent number density of holes $p(t)$ must be equal to the total density of electrons across the conduction band and traps, $n(t)+n_T(t)$. The fitting was performed over the temporal range indicated by black solid lines in Figure S1 and S3 in order to avoid uncertainty caused by low signal at later times.

S2 Charge-carrier dynamics in $FA_{0.83}Cs_{0.17}PbBr_{0.6}I_{2.4}$

S2.1 Time-resolved microwave conductivity

Figure S1 shows the photoconductivity transients measured with the TRMC system described in the Experimental Section of the main text for a thin film of $FA_{0.83}Cs_{0.17}PbBr_{0.6}I_{2.4}$, deposited on a z-cut crystalline quartz disk substrate. The conductivity data is shown by solid, coloured lines. The fluence of the laser excitation was varied with a neutral density filter wheel between 0.1 and 5.9 $\mu J/cm^2$ (darker colour of the transients indicates lower fluence). The sample temperature was varied using a cold finger cryostat and is indicated in each of the sub-figures in coloured text. The fits to the transients, described in Section S1, are shown in black solid lines on top of the data, and extracted decay constants are shown in Table S1. We note that the monomolecular recombination rate k_M (associated e.g. with phonon-mediated recombination and traps that do not retain charge carriers) was not necessary to describe satisfactorily the transients for $FA_{0.83}Cs_{0.17}PbBr_{0.6}I_{2.4}$ and was therefore set to 0.

The photoconductivity traces were used to calculate the relative change of effective charge-carrier sum mobility with temperature, based on Equation 2 in the main text. A value proportional to the mobility was extracted from a linear fit to the photoconductivity magnitude at time=0 plotted against excitation fluence, as detailed in Section S4.1 of the SI for the photoconductivity data recorded for the $CsPbBr_3$ perovskite. The calculated value was subsequently normalised to the mobility obtained from OPTP measurement at room temperature, measured as explained in Section S5.2. The resultant dependence of charge-carrier mobility with temperature is shown in Figure 2 of the main text.

Table S1: Charge-carrier recombination parameters obtained from fitting photoconductivity traces recorded for a $FA_{0.83}Cs_{0.17}PbBr_{0.6}I_{2.4}$ thin film, shown in Figure S1.

Temperature (K)	k_T $(10^6 s^{-1})$	k_M $(10^6 s^{-1})$	k_{Bi} $(10^{-9} s^{-1} cm^3)$	k_E $(10^{-9} s^{-1} cm^3)$
5	0	0	0.604	2.22
10	0	0	0.606	2.27
15	0	0	0.620	2.59
20	0	0	0.689	2.71
35	0	0	0.715	2.92
50	0	0	0.693	2.79
65	0	0	0.631	127.66
80	0	0	0.562	42.68
95	0	0	0.510	21.81
96	0	0	0.498	21.86
110	1.70	0	0.331	23.74
125	2.17	0	0.266	26.85
140	2.61	0	0.214	23.85
155	2.86	0	0.180	36.27
170	3.36	0	0.168	21.97
185	3.01	0	0.135	300.00
200	3.12	0	0.110	5.10
215	3.04	0	0.097	2.48
230	3.86	0	0.086	11.45
245	4.64	0	0.082	14.47
260	5.77	0	0.079	4.94
275	7.16	0	0.081	2.81
290	7.97	0	0.079	2.41
296	8.53	0	0.076	1.79

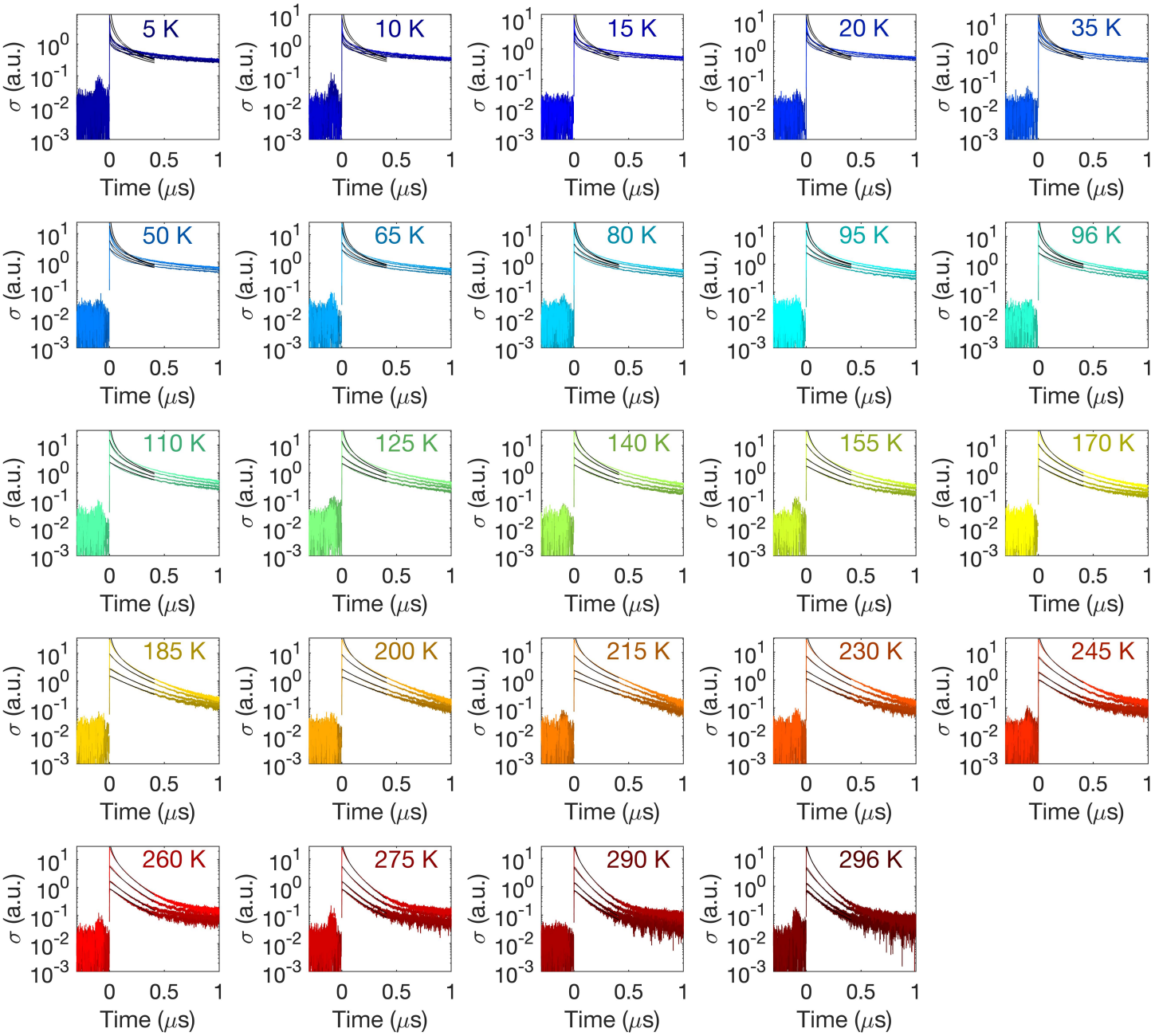

Figure S1: Transients of photoinduced conductivity σ for a thin film of $FA_{0.83}Cs_{0.17}PbBr_{0.6}I_{2.4}$. The film was excited with short laser pulses (35 fs pulse duration) of 670 nm central wavelength with excitation fluences varied between 0.1 (darkest lines) and 5.9 $\mu J/cm^2$ (lightest line), shown respectively as the increasing amplitude transients in each plot. The sample temperature is indicated in each panel and black solid lines represent fits to the conductivity transients as explained in the text. The colours of the plots correspond to the colours of the datapoints used in Figure 2 of the main text.

S2.2 Time-resolved photoluminescence

The time-resolved photoluminescence traces measured in situ, at the same time as the time-resolved microwave transients, for $FA_{0.83}Cs_{0.17}PbBr_{0.6}I_{2.4}$ (as explained in the Experimental Section of the main text) are shown in **Figure S2**. Using the decay parameters extracted from fits to photoconductivity data and shown in Table S1, we calculated numerically the charge-carrier density using coupled rate Equations 1a and 1b in the main text, and subsequently used Equation 3 of the main text ($I_{PL} \propto k_{Bi} np$) to predict the photoluminescence decay transients. This prediction is plotted as black solid lines on top of the data transients (coloured lines) in Figure S2 and shows good agreement with the observed transients for a wide range of sample temperatures.

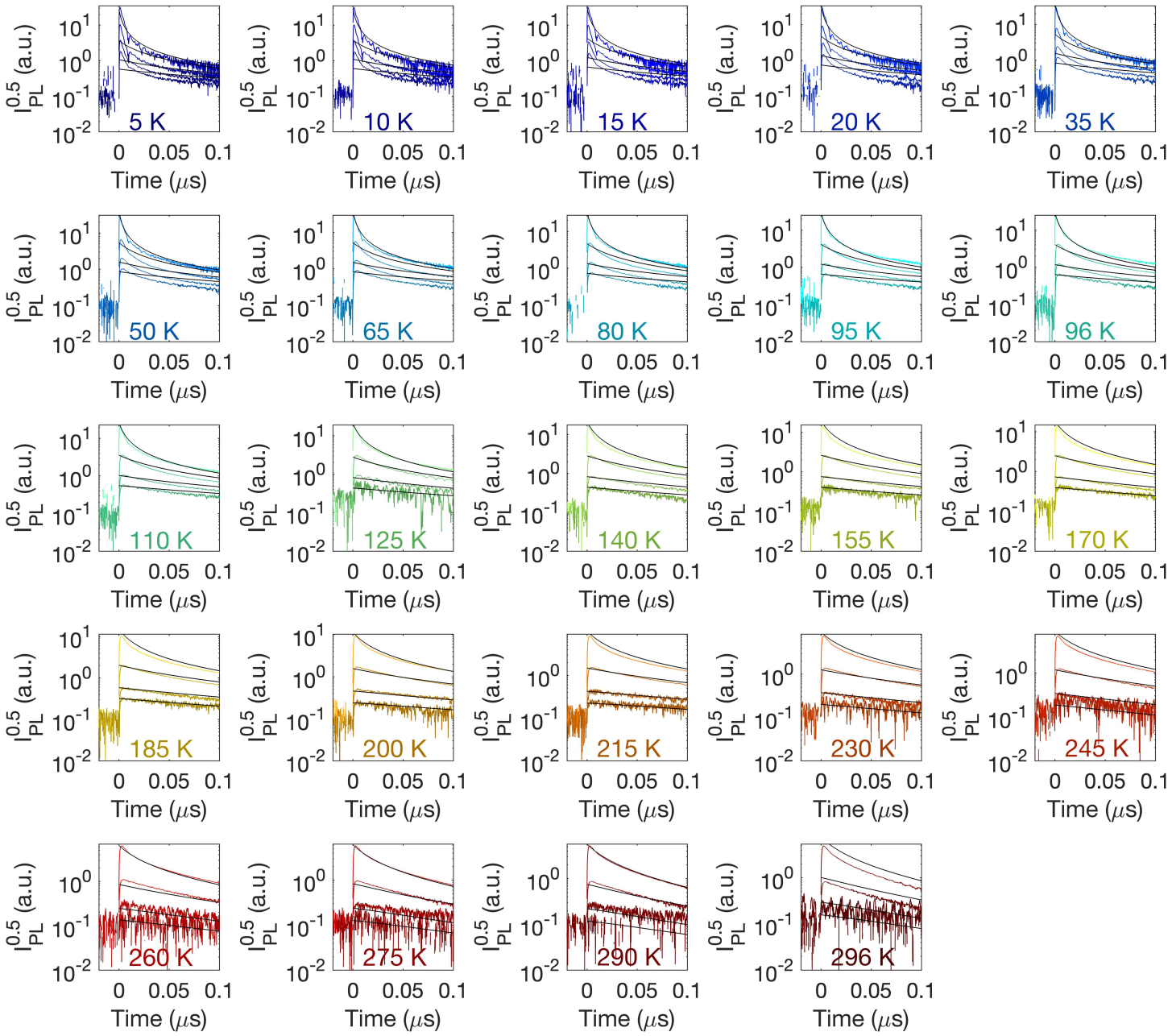

Figure S2: Square root of time-resolved photoluminescence (TRPL) intensity transients for a thin film of $FA_{0.83}Cs_{0.17}PbBr_{0.6}I_{2.4}$. The film was excited with short laser pulses (35 fs pulse duration) with 670 nm central wavelength with excitation fluences varied between 0.1 (darkest lines) and 5.9 $\mu J/cm^2$ (light-coloured lines), shown respectively as the increasing amplitude transients in each plot. The sample temperature is indicated in each panel and black solid lines represent predicted TRPL traces as explained in the text. The colours of the plots correspond to the colours of the datapoints used in Figure 2 of the main text.

S3 Charge-carrier dynamics in $MAPbI_3$

S3.1 Time-resolved microwave conductivity

Figure S3 shows the photoconductivity transients measured in the same way as described above for a thin film of $MAPbI_3$. The conductivity transients are shown as solid, coloured lines. The fluence of the laser excitation was varied between 0.1 and 6.5 μJ/cm^2 (darker colour of the transients indicates lower fluence) as seen by increasing amplitude of the transients. The sample temperature is indicated in each of the sub-figures in coloured text. The fits to the transients are shown as black solid lines on top of the data and extracted decay constants are listed in Table S2.

Table S2: Charge-carrier recombination parameters obtained from fits to photoconductivity transients recorded for a $MAPbI_3$ thin film, shown in Figure S3.

Temperature (K)	$k_T(10^6 s^{-1})$	$k_{\mathrm{M}}(10^6 s^{-1})$	$k_{\mathrm{Bi}}(10^{-9} s^{-1} cm^3)$	$k_{\mathrm{E}}(10^{-9} s^{-1} cm^3)$
40	0.00	0.00	1.162	7.58
50	0.00	0.00	1.09	2.79
60	0.00	0.00	0.87	1.63
70	0.00	0.00	0.91	2.18
80	0.00	0.09	0.840	2.49
95	0.00	0.56	0.844	2.80
110	0.00	0.09	0.783	2.30
125	0.00	0.00	0.749	1.91
140	0.00	0.00	0.659	1.30
155	0.00	1.28	0.180	0.49
170	0.00	1.51	0.153	0.40
185	1.17	0.68	0.141	0.00
200	1.24	0.73	0.124	0.00
215	0.61	1.59	0.120	0.00
230	0.00	2.25	0.124	0.04
245	0.00	2.78	0.134	0.00
260	0.00	3.47	0.164	0.00
275	4.27	2.19	0.166	0.93
295	5.00	3.53	0.227	1.11

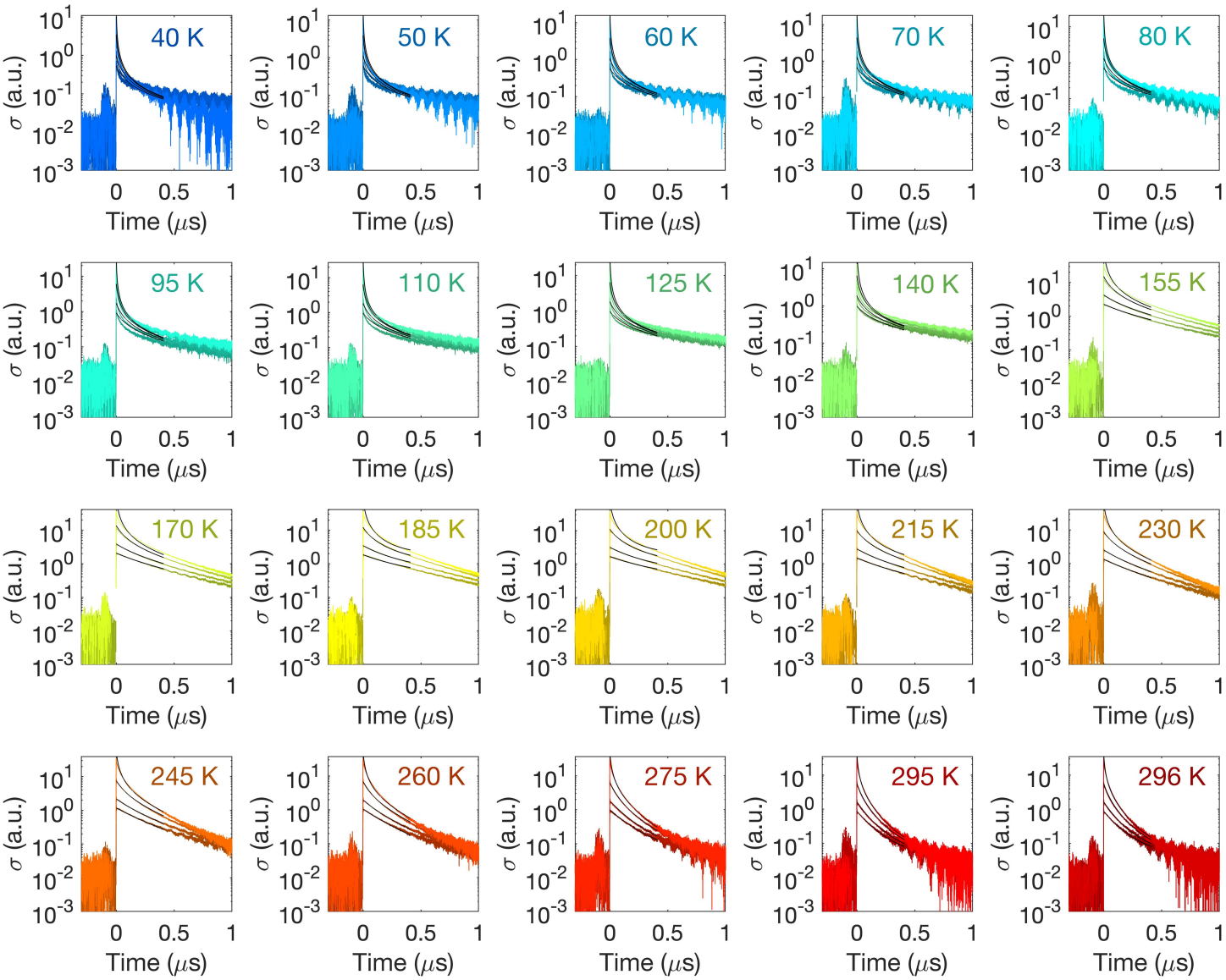

Figure S3: Transients of the photoinduced conductivity σ recorded for a $MAPbI_3$ thin film. The film was excited with short laser pulses (35 fs pulse duration) of 670 nm central wavelength with excitation fluence varied between 0.1 (darkest lines) and 6.5 $\mu J/cm^2$ (light-coloured lines), shown respectively as the increasing amplitude transients in each plot. The sample temperature is indicated in each panel and black solid lines represent fits to the conductivity as explained in the text.

S3.2 Time-resolved photoluminescence

The time-resolved photoluminescence traces measured in situ for $MAPbI_3$ are shown in **Figure S4**. Predictions of the PL transients, calculated as described above, are shown as solid black lines.

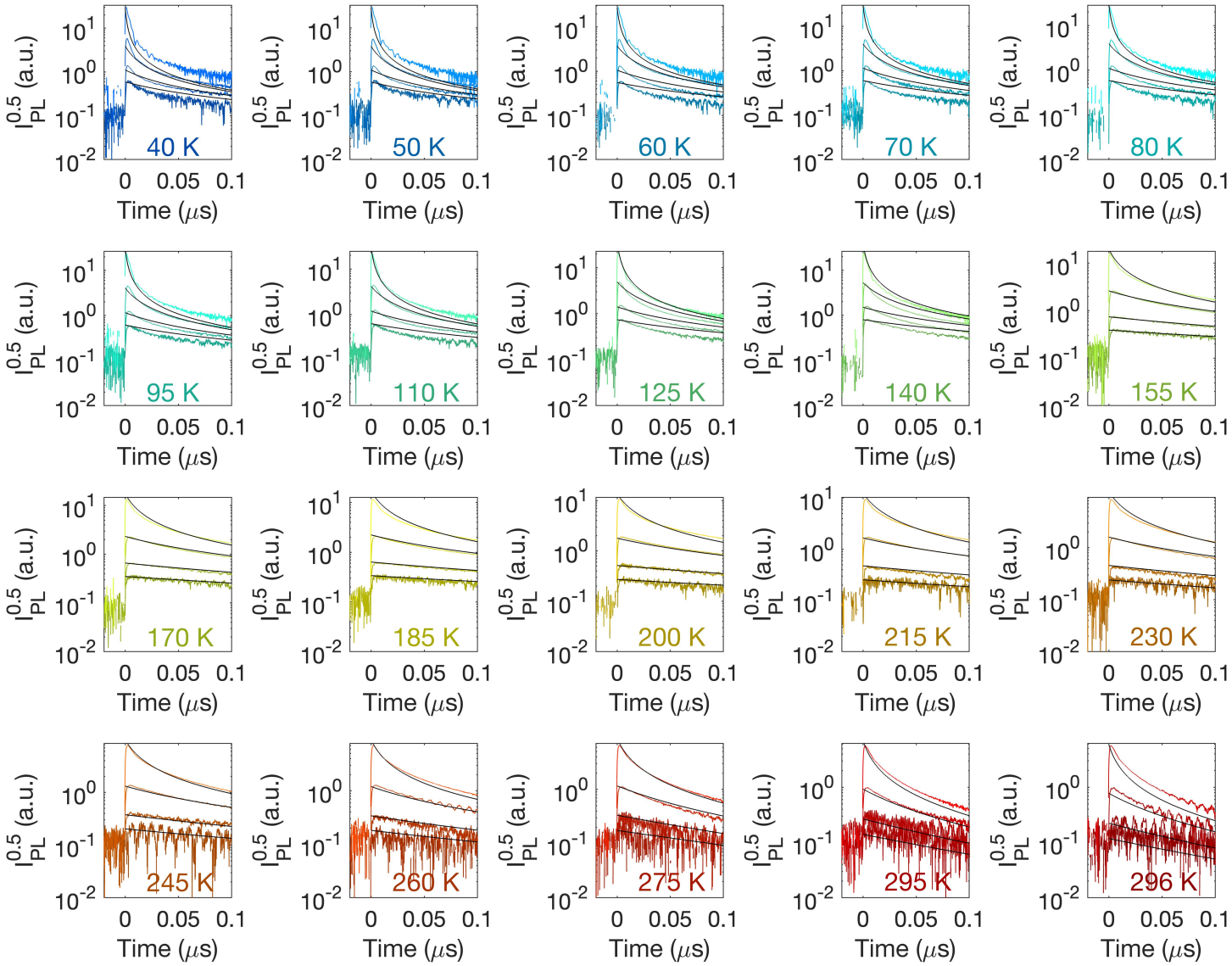

Figure S4: Square root of the time-resolved photoluminescence intensity transients recorded for a thin film of $MAPbI_3$. The film was excited with short laser pulses (35 fs pulse duration) of 670 nm central wavelength with excitation fluence varied between 0.1 (darkest lines) and 6.5 $\mu J/cm^2$ (light-coloured lines), shown respectively as the increasing amplitude transients in each plot. The sample temperature is indicated in each panel and black solid lines represent predicted TRPL traces as explained in the text. The colours of the plots correspond to the colours of the datapoints used in Figure 3a of the main text.

S4 Charge-carrier dynamics in $CsPbBr_3$

Figure S5 shows the photoconductivity transients for a $CsPbBr_3$ thin film, measured in the same way as described above, but with laser pulses of 400 nm central wavelength used to photoexcite the film. The conductivity is shown as solid, coloured lines and is normalised to 1 at the peak for each excitation fluence. The fluence of the laser excitation was varied between 0.4 and 12.4 $\mu J/cm^2$ (darker colour of the transients indicates lower fluence). The sample temperature is indicated in each of the sub-figures in coloured text. The transients measured at high temperatures show no fluence dependence and follow the dynamics of electrons being released from the traps [3], as explained in the main text. The low-temperature transients exhibit a power-law decay, evident from the apparent linearity when data are plotted on a double-logarithmic scale, which stems from the de-trapping of charge carriers in band tail states [4, 3] (as described in the main text) and shows fluence dependence caused by an increase of electron-hole recombination strength at low temperatures.

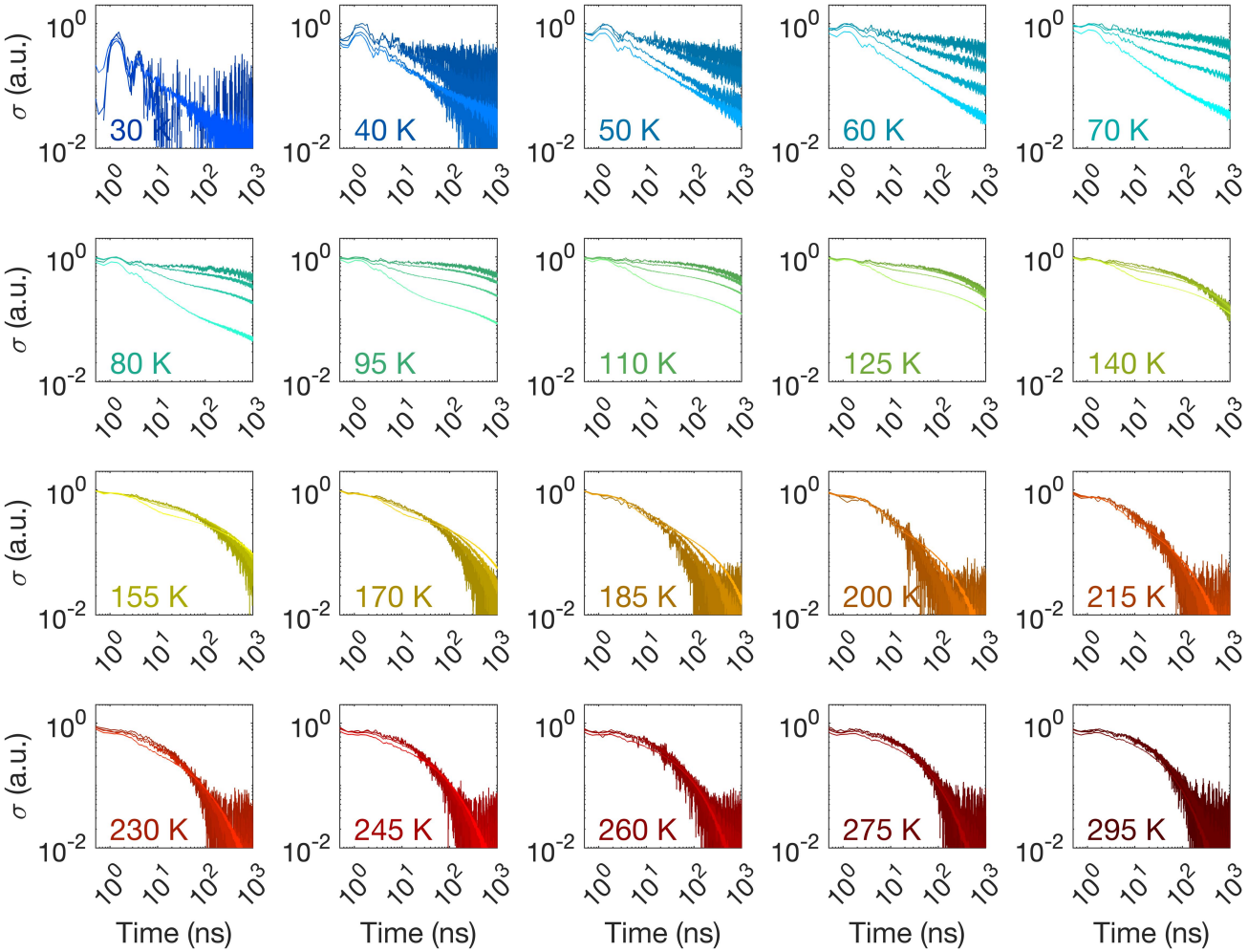

Figure S5: Transients of photoinduced conductivity σ recorded for a thin film of $CsPbBr_3$. The film was excited with short laser pulses (35 fs pulse duration) of 400 nm central wavelength with excitation fluence varied between 0.4 (darkest lines) and 12.4 $\mu J/cm^2$ (light-coloured lines). The sample temperature is indicated in each panel.

S4.1 Mobility calculation

The dependence of the effective electron-hole sum mobility on temperature was calculated for all three perovskite compositions in the same way, as follows. Based on Equation 2 in the main text, $\sigma = \frac{\mu_{cc}}{2}(n+p)$, the sum mobility is the proportionality constant between photoinduced conductivity and excited charge-carrier pair density. **Equation S1** shows that the charge-carrier density just after photoexcitation (at

time=0) is proportional to the photon–to–charge-carrier branching ration ϕ and excitation fluence F. Therefore, a quantity proportional to the effective electron-hole sum mobility ($\phi\mu_{cc}$) can be calculated from the slope of the linear fit to the photoconductivity magnitude at time=0 plotted against excitation fluence. Examples of such fits to the three lowest fluences are shown in **Figure S6** for the $CsPbBr_3$ thin film. The highest fluence datapoint (at 12.4 $\mu J/cm^2$) was not used in order to avoid the effects of fast photoconductivity decay within the time resolution of the system at high excitation densities. The slopes of such fits obtained for each of the samples were scaled such that the room-temperature value coincided with the mobility value obtained from OPTP measurements at room temperature (see Section S5.2). The normalised values were used to demonstrate the temperature dependence of effective charge-carrier sum mobility presented in Figures 2 and 4 of the main text as well as **Figure S11** of the SI.

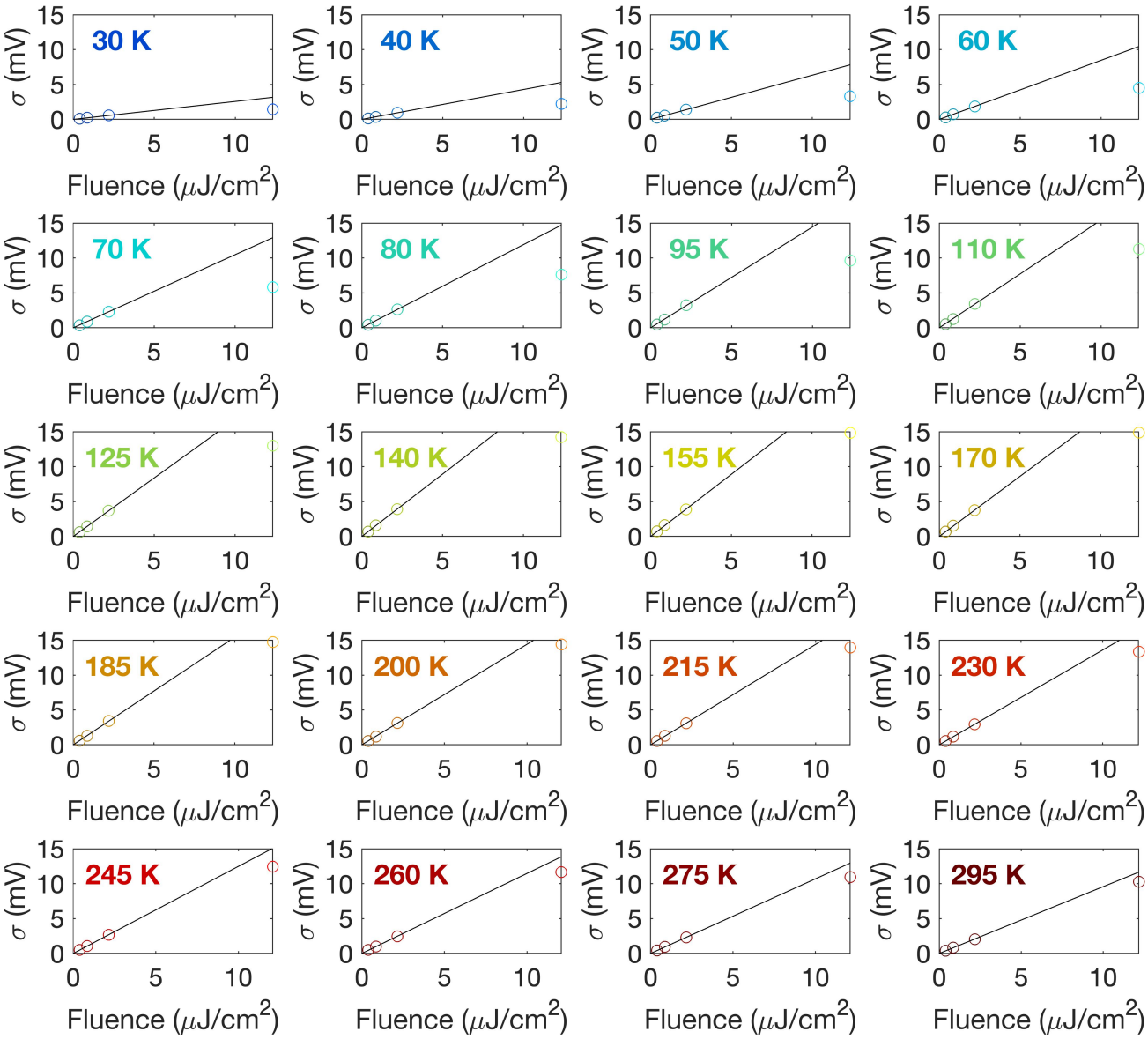

Figure S6: Peak microwave photoconductivity values, shown as the maximal signal measured by the acquisition system (described in the Experimental Section of the main text) in mV, plotted against excitation fluence for a thin film of $CsPbBr_3$ perovskite. The data is shown as open circles, the sample temperature is indicated in each subplot and the black solid lines represent the linear fit to the three lowest fluences. The colours of the plots correspond to the colours of the datapoints used in Figure 4d of the main text.

S5 Optical-pump–THz-probe measurements

S5.1 Temperature dependence: $FA_{0.83}Cs_{0.17}PbBr_{0.6}I_{2.4}$

Temperature-dependent optical-pump–terahertz-probe measurements were performed as described in the Experimental Section of the main text. **Figure S7** shows the OPTP transients measured for a thin film of $FA_{0.83}Cs_{0.17}PbBr_{0.6}I_{2.4}$ perovskite at temperatures indicated in each subplot. The open circles represent measured data at fluences of 72.9 μJ/cm^2, 25.5 μJ/cm^2, and 9.1 μJ/cm^2.

The temperature-dependent mobility (shown in Figure 2f of the main text by the solid magenta line) was calculated using Equation 4 in the main text, with the peak value $\Delta T/T$ extracted at the lowest fluence from traces shown in Figure S7. The photoexcited charge-carrier density was calculated using Equation S1.

To fit the transients with the charge-carrier recombination model, we note that within the first nanosecond of the decay (range of OPTP measurements), monomolecular recombination rates for $FA_{0.83}Cs_{0.17}PbBr_{0.6}I_{2.4}$ (see Table S1) do not contribute significantly to the decrease of the charge-carrier population (e.g. for a monoexponential decay with a rate of k_T=8×10^{6}s^{-1}, $e^{-k_T t}$=0.992 at t=1 ns). Therefore, only bimolecular recombination is taken into account, simplifying the rate Equations 1a and 1b in the main text to the simple differential equation,

$$\frac{dn}{dt} = -k_{\mathrm{Bi}} np = -k_{\mathrm{Bi}} n^2 \,, \tag{S2}$$

where $n = p$ are the electron- and hole- number densities, equal to each other because of the lack of single-carrier trapping on the timescale of the measurement. **Equation S2** has an analytical solution of the form

$$n(t) = \frac{n_0}{k_{\mathrm{Bi}} n_0 t + 1} \,, \tag{S3}$$

where n_0 is the charge-carrier population at time=0. We note that Figure S7 shows an accelerated decay within the first few tens of picoseconds at low temperatures and high excitation densities that we attribute to amplified spontaneous emission (ASE), given the line-narrowing observed in the corresponding PL spectra (see discussion in the main text). In order to avoid including the contribution of ASE to the radiative recombination rate [5, 6], **Equation S3** was fitted to data from 65 ps after photoexcitation onwards. The initial charge-carrier density at 65 ps, used to fit Equation S3 to data, was calculated by dividing the photoconductivity value at this time delay (Equation 4 from the main text) by the charge-carrier mobility and charge, $\mu_{\mathrm{cc}} e$, calculated as described above.

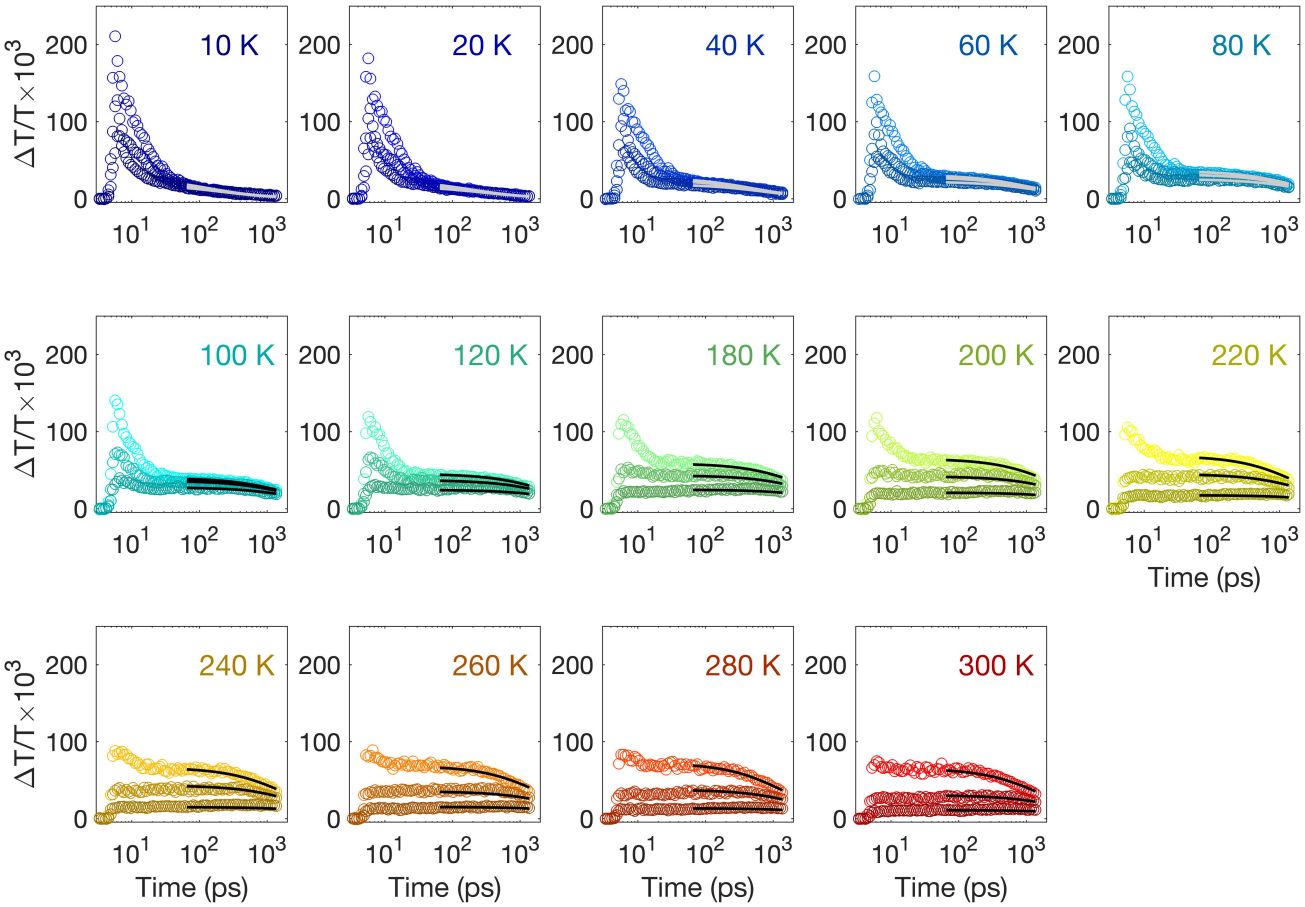

Figure S7: Transients of photoinduced conductivity recorded for a thin film of $FA_{0.83}Cs_{0.17}PbBr_{0.6}I_{2.4}$ with the optical-pump–THz-probe method. The film was excited with short laser pulses (35 fs pulse duration) of 670 nm central wavelength with excitation fluence varied between 9.1 μJ/cm^2 (darkest circles) and 72.9 μJ/cm^2 (light-coloured circles), shown as increasing amplitude transients. The sample temperature is indicated in each panel. The solid lines show fits of Equation S3 to data as outlined in the text.

S5.2 Room temperature OPTP

Room temperature OPTP experiments were performed as described in the Experimental Section of the main text, and the photoconductivity traces are shown in **Figure S8** for (a) $FA_{0.83}Cs_{0.17}PbBr_{0.6}I_{2.4}$,(b) $MAPbI_3$, and (c) $CsPbBr_3$ thin films. In Figure S8 a and b, open circles represent the photoconductivity transients measured using excitation fluences of 14.2 μJ/cm^2, 3.6 μJ/cm^2, and 0.8 μJ/cm^2 (light, medium and dark colour of the circles), shown respectively as increasing amplitude of the transients. Data shown in Figure S8 c were measured at fluences of 31.9 μJ/cm^2, 8.0 μJ/cm^2, and 2.1 μJ/cm^2, labelled in the same way. The photoconductivity of $CsPbBr_3$ measured at the excitation fluence of 8.0 μJ/cm^2 is also plotted in Figure 4a of the main text, as it was acquired under similar conditions to the TRMC and PL data (measured at 12.4 μJ/cm^2) in the same figure. The black solid lines in Figure S8 c represent the fits to OPTP data, generated using the model described in Section 2.5 of the main text. The model is expressed by the coupled differential equations,

$$\begin{cases} \frac{\partial n}{\partial t} = -k_T n - k_{\mathrm{Bi}} np \\ \frac{\partial n_T}{\partial t} = k_T n - n_t \beta (\frac{1}{k_{\mathrm{KWW}}})^{-\beta} t^{\beta-1} \end{cases}, \tag{S4}$$

where β is the stretching exponent, k_{KWW} is the characteristic rate of the trap-emptying mechanism and the remaining variables are defined in the same way as in Section 2.2 of the main text. We note that in absence of other dynamic processes, the decay rate $\beta(\frac{1}{k_{\mathrm{KWW}}})^{-\beta} t^{\beta-1}$ leads to a stretched exponential decay $\propto e^{-(k_{\mathrm{KWW}} t)^{\beta}}$ [7, 8]. We found that fits with the trapping rate of $k_T = 1.53 \times 10^9 \mathrm{s}^{-1}$, bimolecular recombination constant of $k_{\mathrm{Bi}} = 1.46 \times 10^{-9} \mathrm{s}^{-1}\mathrm{cm}^3$, characteristic Kohlrausch-Williams-Watts rate of

$k_{\mathrm{KWW}} = 25.94 \times 10^6 \mathrm{s}^{-1}$, and stretching parameter $\beta = 0.71$ reproduce both the fluence-dependent OPTP traces and the TRMC trace in Figure 4a in the main text with high accuracy.

The effective electron-hole sum mobilities indicated in Figure S8 were calculated by fitting a linear function to the value of $\Delta T/T$ at time=0 of the transients plotted against the fluence. Combining Equation 4 in the main text with Equation S1, the slope of the fitted line was used to calculate the mobility and the 90% confidence interval of the fit was used to evaluate the uncertainty shown in the figure.

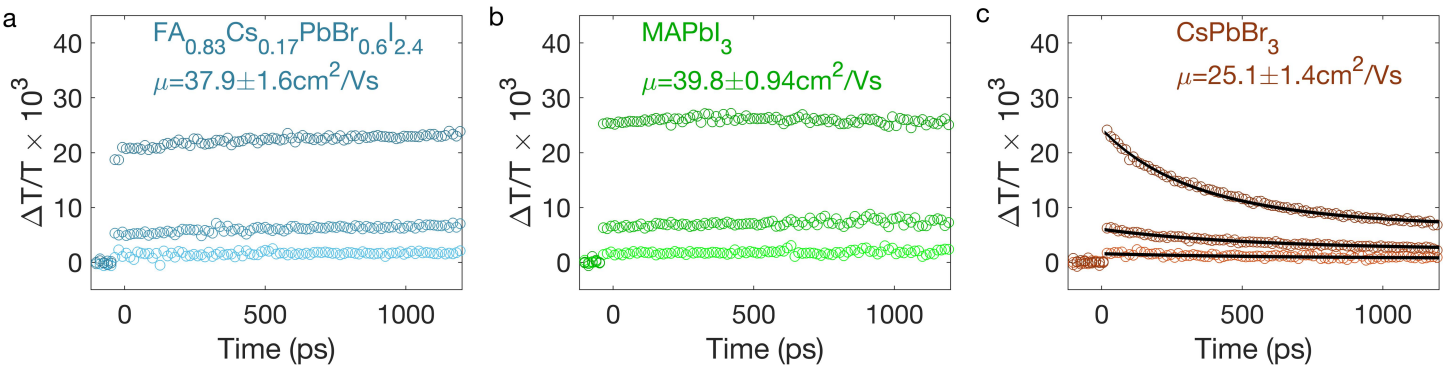

Figure S8: Room temperature OPTP traces for (a) $FA_{0.83}Cs_{0.17}PbBr_{0.6}I_{2.4}$, (b) $MAPbI_3$, and (c) $CsPbBr_3$ thin films, measured at fluences of 14.2 μJ/cm^2, 3.6 μJ/cm^2, and 0.8 μJ/cm^2, for light, medium and dark colour of the circles, respectively in (a) and (b), and at 31.9 μJ/cm^2, 8.0 μJ/cm^2, and 2.1 μJ/cm^2 in (c). The black solid lines in (c) show fits to data, described in the text. The effective electron-hole sum mobilities were calculated through the linear fit to prompt photoconductivity plotted against fluence, as described in the text, and the uncertainty represents the confidence intervals of the fit.

S6 Excitonic effects in $FA_{0.83}Cs_{0.17}PbBr_{0.6}I_{2.4}$ and $CsPbBr_3$

S6.1 Absorption edge analysis

The absorption spectra were measured as described in the Experimental Section in the main text. The onset in the absorption coefficient spectrum was fitted using Elliott's model, which describes the absorption of a semiconductor near its band edge [9]. The theory expresses the energy-dependent absorption coefficient as:

$$\alpha(E) = \alpha_{\mathrm{X}}(E) + \alpha_{\mathrm{C}}(E)$$

The bound exciton contribution α_{X} has the form:

$$\alpha_{\mathrm{X}}(E) = \frac{b_0}{E} \sum_{n=1}^{\infty} \frac{4\pi E_{\mathrm{B}}^{3/2}}{n^3} \delta\left(E - \left[E_{\mathrm{g}} - \frac{E_{\mathrm{B}}}{n^2}\right]\right)$$

where b_0 is a constant of proportionality that incorporates the electric dipole transition matrix element between the valence and conduction band. α_{X} is formed of the weighted sum of contributions from the exciton states with positive integer quantum number n and energies $E_{\mathrm{g}} - \frac{E_{\mathrm{B}}}{n^2}$, where E_{g} is the band gap energy and E_{B} is the exciton binding energy.

The contribution from the electron-hole continuum states $\alpha_{\mathrm{C}}(E)$ has the form

$$\alpha_{\mathrm{C}}(E) = \frac{b_0}{E}\left[\frac{2\pi\sqrt{\frac{E_{\mathrm{B}}}{E-E_{\mathrm{g}}}}}{1-\exp(-2\pi\sqrt{\frac{E_{\mathrm{B}}}{E-E_{\mathrm{g}}}})}\right] c_0^{-1}\mathrm{JDoS}(E)$$

where the joint density of states is given by $\mathrm{JDoS}(E) = c_0\sqrt{E-E_{\mathrm{g}}}$ for $E > E_{\mathrm{g}}$ and 0 otherwise, and the joint density of states constant $c_0 = \frac{1}{(2\pi)^2}\left(\frac{2\mu}{\hbar^2}\right)^{3/2} \times 2$, where μ is the reduced effective mass of the electron-hole system. The term in square brackets is the Coloumbic enhancement factor, which increases the absorption from the continuum states above the square-root form of the JDoS for a direct-gap semiconductor

as a result of the Coloumbic attraction between the unbound electrons and holes.
The linear combination of the contributions from the excitonic and continuum states, $\alpha(E)$, is then convolved with a normal distribution broadening function which has a mean 0 and standard deviation Γ. The broadening function represents the homogeneous broadening caused by electron-phonon coupling, disorder and local fluctuations of the stoichiometry of the material, and is mathematically denoted by $g(E) = N(0, \Gamma^2)$.

The Elliott function, $f_{\text{Elliott}} = \alpha(E, E_{\text{g}}, E_{\text{B}}) \otimes N(0, \Gamma^2)$, (where convolution is represented by the symbol $\otimes$) was fitted to the absorption onsets for the three metal halide perovskite thin films by a least-squares minimisation method. The resultant Elliott fits are shown in Figure 4c in the main text for $FA_{0.83}Cs_{0.17}PbBr_{0.6}I_{2.4}$ and $CsPbBr_3$ perovskites and in Figure S9 for $MAPbI_3$. The extracted fit parameters are listed in Table S3.

Table S3: Bandgap energy E_{g}, exciton binding energy E_{B} and broadening parameters Γ, extracted from Elliott fits to the absorption onsets of three perovskite compositions listed in the table.

Composition	$E_g(eV)$	E_B (meV)	Γ (meV)
$FA_{0.83}Cs_{0.17}PbBr_{0.6}I_{2.4}$	1.67	13	33
$MAPbI_3$	1.64	10	29
$CsPbBr_3$	2.44	37	27

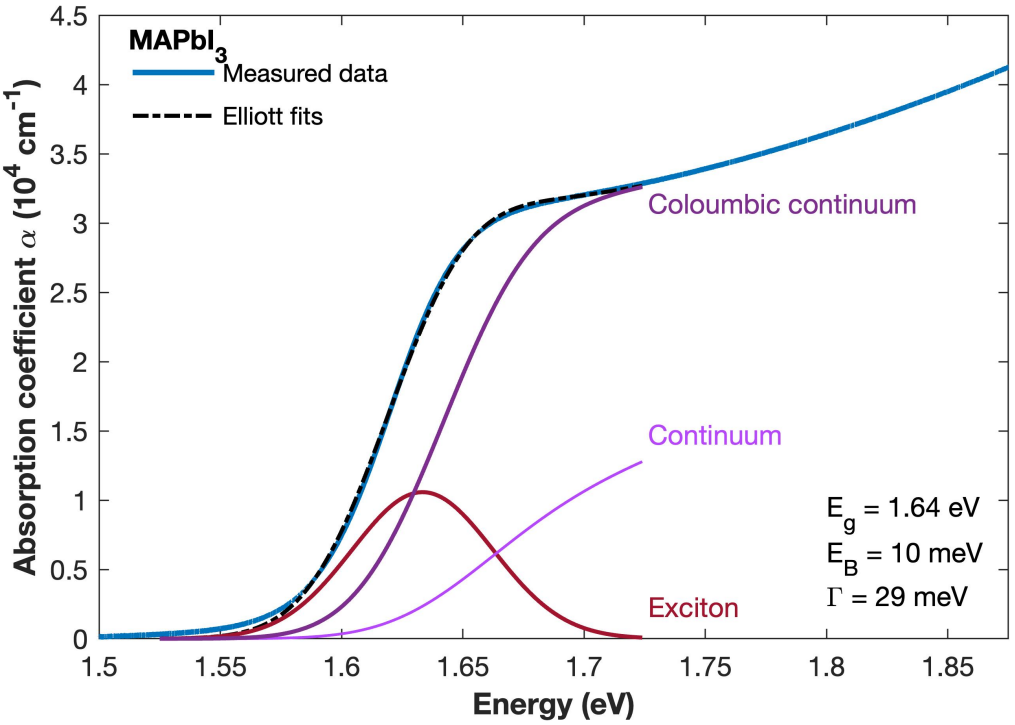

Figure S9: Absorption spectrum of $MAPbI_3$ thin film, acquired as described in the experimental chapter of the main text, shown in a blue solid line. The contributions to the Elliott fit (black dashed line) from the excitonic absorption, band-to-band continuum absorption and coulombic interactions are shown in red, magenta and purple solid lines, respectively.

S6.2 Branching ratio calculation

In order to verify to what extent exciton formation affects the temperature dependence of the effective charge-carrier mobility in metal-halide perovskites, we calculated the photon–to–free-carrier branching ratio, ϕ, using the Saha–Langmuir equation [1, 10, 11, 12],

$$\frac{\phi^2}{1-\phi} = \frac{1}{n}\left(\frac{2\pi m_{\text{red}} kT}{h^2}\right)^{3/2} e^{-E_B/kT}, \tag{S5}$$

where n is the charge-carrier density, m_{red} is the reduced mass of the exciton, k is the Boltzmann constant, h is the Plank constant, T is the temperature, and E_B is the exciton binding energy.

Using **Equation S5**, we calculated the dependence of the branching ratio on temperature for $FA_{0.83}Cs_{0.17}PbBr_{0.6}I_{2.4}$ and $CsPbBr_3$, using the respective exciton binding energies extracted from the Elliott fits, and plotted it in Figure S10 as a function of temperature. The solid lines represent the fraction of photons converted to free charge carriers for the two compositions labelled in the figure. We note that in $FA_{0.83}Cs_{0.17}PbBr_{0.6}I_{2.4}$, with relatively low exciton binding energy E_B =13 meV, the fraction of free charge carriers falls below 0.5 only at temperatures below 60 K, implying that excitonic effects do not significantly reduce the effective free charge mobility for a large range of temperatures. Meanwhile, for $CsPbBr_3$ with exciton binding energy of E_B =37 meV, the fraction of free carriers falls below 0.5 at a much higher temperature of 120 K, explaining the reduction of charge-carrier effective mobility seen in the data presented in Figure 4d of the main text.

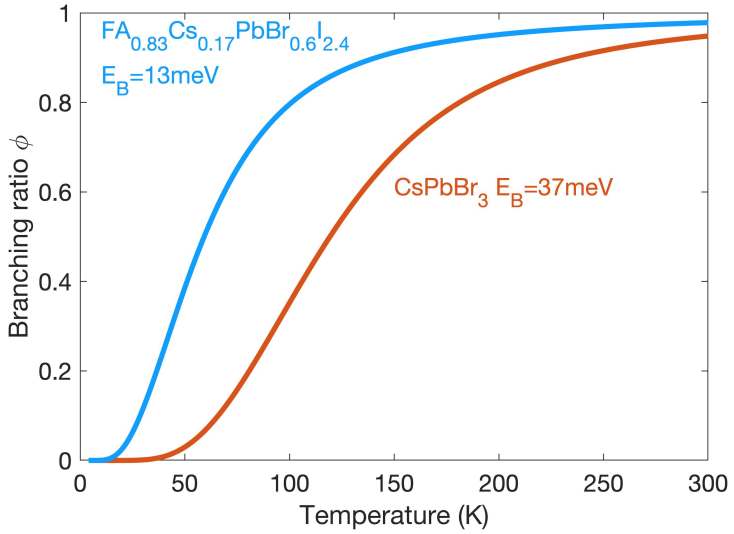

Figure S10: Photon–to–free-carrier branching ratio ϕ predicted by the Saha equation, plotted against sample temperature for an excitation density of $n = 10^{16}\text{cm}^{-3}$, comparable to the densities used in this study, calculated for $FA_{0.83}Cs_{0.17}PbBr_{0.6}I_{2.4}$ (blue) and $CsPbBr_3$ (orange) perovskites. The exciton binding energies E_B, extracted from Elliott fits are shown in the corresponding colours in the figure. A reduced exciton mass of $m_{\text{red}} = 0.15m_e$, where m_e is the electron mass, was used for the calculations [13, 1].

S7 Temperature-dependent mobility trends across the three perovskites

The evolution of the effective electron-hole sum mobility with temperature for the three perovskite compositions is shown in **Figure S11**. For better comparison, we include the data shown in Figure 2f and Figure 4d of the main text here as well. We note that while the evolution of the effective mobility for $FA_{0.83}Cs_{0.17}PbBr_{0.6}I_{2.4}$ (Figure S11a) and $CsPbBr_3$ (Figure S11c) can be explained by the limited time resolution of the system (because of charge-carrier recombination and therefore lowering of conductivity within the time resolution), combined with excitonic effects (as summarised in Section S6.2), the behaviour of the effective mobility in $MAPbI_3$ (Figure S11b) cannot be solely attributed to these effects. Instead, we suggest that the drop in charge-carrier mobility just below 150 K, the temperature of the structural phase transition, visible in Figure S11b is caused by the phase inhomogeneity of the film arising from inclusions of the tetragonal phase in an otherwise orthorhombic crystal. A further decrease in the charge-carrier mobility below 100 K can be correlated with the appearance of sub-bandgap emission, shown in Figure 3b of the main text and **Figure S12**, indicating that charge carriers localise in energetic trap bands just below the band-edge, which reduces the total charge-carrier conductivity of the photoexcited material.

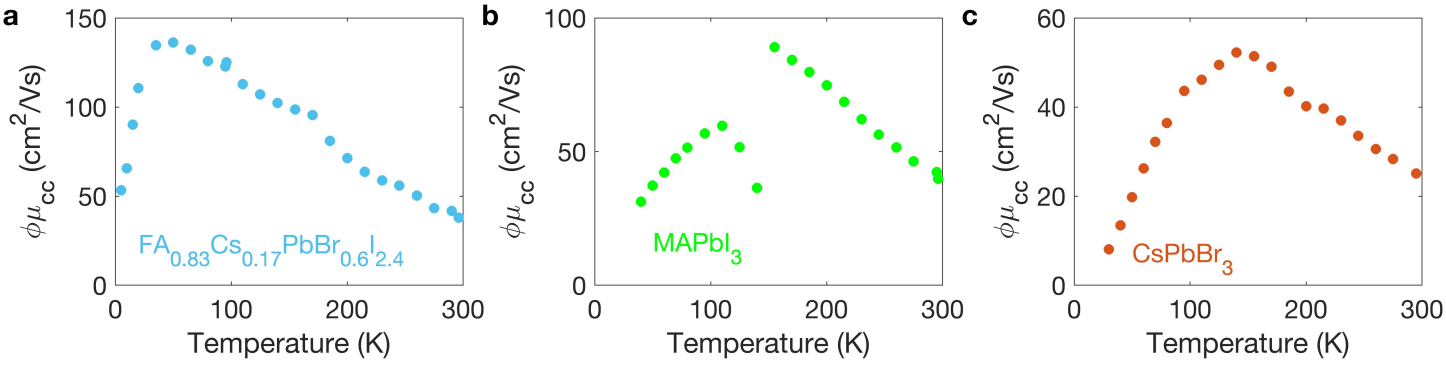

Figure S11: Evolution of effective charge-carrier sum mobility for three perovskite compositions. The effective mobility of a) $FA_{0.83}Cs_{0.17}PbBr_{0.6}I_{2.4}$,b) $MAPbI_3$, and c) $CsPbBr_3$, is calculated as described in Section S4.1.

S8 Photoluminescence spectra of $MAPbI_3$

The evolution of the PL emission spectrum of $MAPbI_3$ with temperature is shown for 4 different excitation fluences in Figure S12. We note that while at the low fluence of 0.1μJ/cm^2, long wavelength, sub-bandgap emission dominates the spectra for temperatures below 150 K, the higher energy band-to-band transition becomes the main radiative recombination pathway at the high excitation fluence of 6μJ/cm^2. This is likely because the tail states are saturated by photoexcited charge carriers present in high densities [4]. Because of the low temperature, suppressed electron-phonon coupling will induce narrow emission linewidths, once band-to-band recombination becomes dominant.

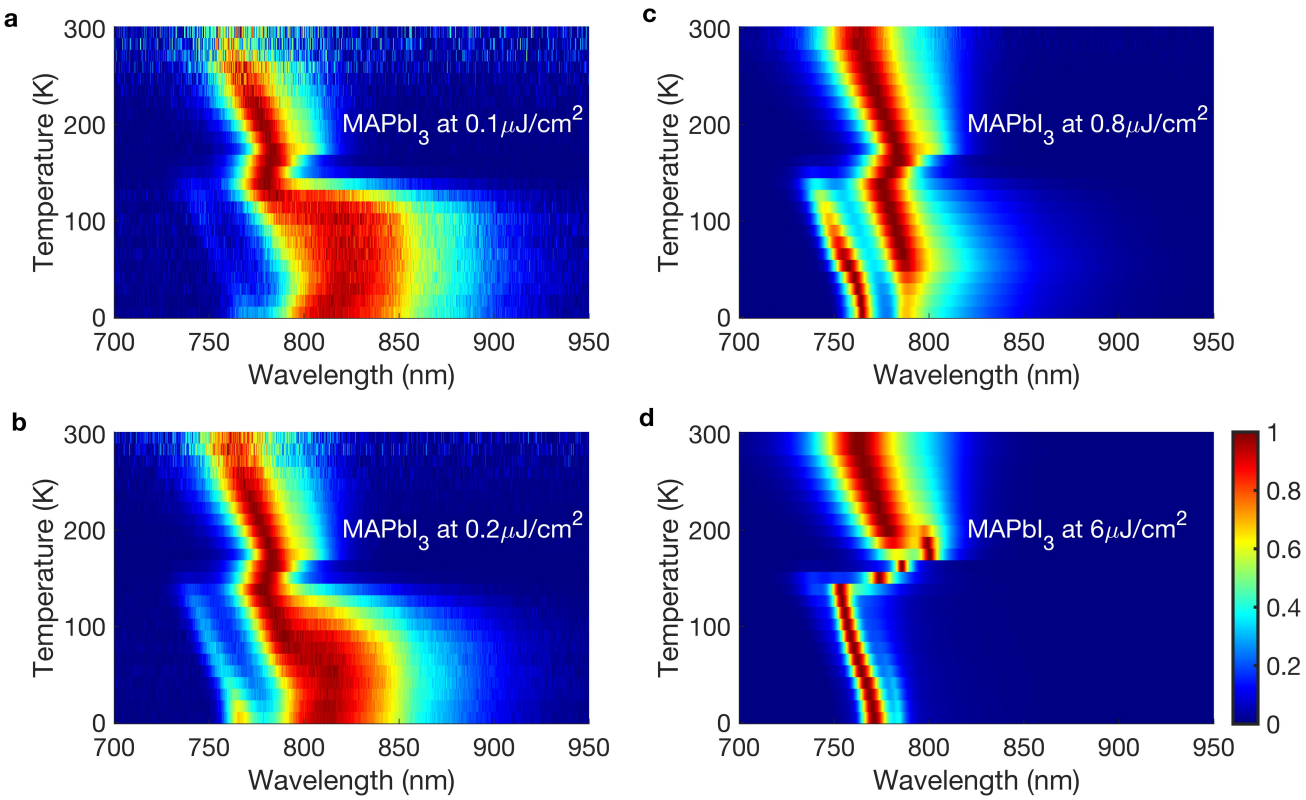

Figure S12: Evolution of photoluminescence spectra recorded for a $MAPbI_3$ thin film with temperature, measured for the excitation fluences indicated in the plots. The spectra were normalised to 1 at the peak emission for each temperature. The spectra were acquired as described in the Experimental Section of the main text.

References

[1] V. D'innocenzo, G. Grancini, M. J. Alcocer, A. R. S. Kandada, S. D. Stranks, M. M. Lee, G. Lanzani, H. J. Snaith, A. Petrozza, *Nat. Commun.* **2014**, *5* 3586.

[2] C. Wehrenfennig, G. E. Eperon, M. B. Johnston, H. J. Snaith, L. M. Herz, *Advanced materials* **2014**, *26*, 10 1584.

[3] J. Fu, N. F. Jamaludin, B. Wu, M. Li, A. Solanki, Y. F. Ng, S. Mhaisalkar, C. H. A. Huan, T. C. Sum, *Advanced Energy Materials* **2019**, *9*, 12 1803119.

[4] A. D. Wright, R. L. Milot, G. E. Eperon, H. J. Snaith, M. B. Johnston, L. M. Herz, *Advanced Functional Materials* **2017**, *27*, 29 1700860.

[5] R. L. Milot, G. E. Eperon, T. Green, H. J. Snaith, M. B. Johnston, L. M. Herz, *The journal of physical chemistry letters* **2016**, *7*, 20 4178.

[6] S. Yakunin, L. Protesescu, F. Krieg, M. I. Bodnarchuk, G. Nedelcu, M. Humer, G. De Luca, M. Fiebig, W. Heiss, M. V. Kovalenko, *Nature Communications* **2015**, *6*, 1 8056.

[7] F. Alvarez, A. Alegra, J. Colmenero, *Physical Review B* **1991**, *44*, 14 7306.

[8] G. Williams, D. C. Watts, *Transactions of the Faraday Society* **1970**, *66* 80.

[9] R. Elliott, *Physical Review* **1957**, *108*, 6 1384.

[10] R. Cingolani, L. Calcagnile, G. Coli, R. Rinaldi, M. Lomoscolo, M. DiDio, A. Franciosi, L. Vanzetti, G. LaRocca, D. Campi, *JOSA B* **1996**, *13*, 6 1268.

[11] M. N. Saha, *Proceedings of the Royal Society of London. Series A, Containing Papers of a Mathematical and Physical Character* **1921**, *99*, 697 135.

[12] E. M. Hutter, M. C. Gélvez-Rueda, A. Osherov, V. Bulović, F. C. Grozema, S. D. Stranks, T. J. Savenije, *Nature Materials* **2017**, *16*, 1 115.

[13] K. Tanaka, T. Takahashi, T. Ban, T. Kondo, K. Uchida, N. Miura, *Solid State Communications* **2003**, *127*, 9-10 619.